3D modeling of arbitrary cracking in solids using augmented finite element method

CrossMark

M. Naderi [*],[1], N. Iyyer

Technical Data Analysis, Inc. (TDA), 3190 Fairview Park Drive, Suite 650, Falls Church, VA 22042, USA

ARTICLE INFO

ABSTRACT

A three dimensional (3D) augmented finite element method (AFEM) for modeling arbitrary cracking without the need of additional degree of freedom (DoFs) or phantom nodes is presented. Four or three internal nodes are employed to explain displacement jump due to the weak and strong discontinuity. In this method, damage and discontinuity are treated from a weak discontinuity to a strong one without additional degree of freedom and without explicit representation of the crack. A fully condensed elemental equilibrium equations as mathematical exactness in the piece-wise linear sense is explicitly derived within AFEM formulation. The method is implemented in ABAQUS 4-node tetrahedron user element with a local crack tracking method for crack path detection. Through some numerical examples, it is shown that the 3D AFEM can accurately and efficiently crack initiation and propagation.

© 2016 Elsevier Ltd. All rights reserved.

1. Introduction

Accurate assessment of the structural integrity involves the development of complex progressive damage analysis with high-fidelity. Since standard finite element method is not suitable to model strong discontinuity and crack, advanced finite elements and numerical methods are developed to explicitly take into account the cracking and damage in the material, e.g., the generalized finite element method (GFEM), extended finite element method (XFEM) [1–8], phantom node method (PNM) [9–14], augmented finite element method [15–18], and meshless methods [19–25].

The generalized finite element, extended finite element and phantom node methods have been developed based on theory of the partition of unity and in essence introduce additional degree of freedom to account for arbitrary cracking. In the case of individual crack, these methods are mesh independent and effective. The shortcomings in these methods are a) the computational cost is very expensive due to additional degree of freedom, b) multiple crack interactions have to be established in the framework of these methods despite some recent articles to deal with multiple crack interactions [5,26,27]. In this regard approaches such as phase field [28–30] and embedded discontinuity [31–36] are developed to cope with arbitrary interacting cracks. Other emerging methods

for failure analyses include the regularized FEM (RxFEM) of Iarve et al. [37] and the continuum–decohesion FEM by Waas and co-workers [38].

Phase field model introduces an additional nodal DoF to approximate a fracture surface with a continuous phase-field parameter and does not need to algorithmically trace fracture. However, the method is mesh-dependent and requires an extremely refined mesh to resolve the sharp discontinuity across the crack surfaces [39]. In embedded discontinuity method, special shape functions are used to account for the discontinuous crack displacements within an element [35]. Though, the special care must be taken for constructing shape functions orthogonality property to avoid spurious deformation or serious stress locking.

Meshless method which is based on interaction of each node with all its neighbor is another alternative to cope with arbitrary cracking problems in solids. The discrete nature of these mesh-free methods makes it easier in handling multiple crack interaction problems. Some recent advances in meshless method are the use of extrinsically enriched methods based on the partition of unity (PoU) theory [20–22] and the use of weight function enrichment [24,25].

A crack tracing method is a major part of modeling arbitrary cracking and is of particular challenge in simulation of 3D solid's failure. Many algorithms for tracing crack path have been developed [39–54]. Four common crack tracking methods are available including the local tracking method, the non-local tracking method, the global tracking method, and the level set methods. Advantages and shortcomings of the tracking methods are

---

* Corresponding author.
   E-mail addresses: mnaderi@tda-i.com, mnaderi@gwu.edu (M. Naderi).
[1] Adjunct Professor at George Washington University.

summarized in Table 1. More details on crack tracking algorithms are referred to Jager et al. [54]

It is noted that most of the above mentioned tracking methods (non-local, global, level set) may not be suitable for heterogeneous materials such as laminated or textile composites. Hence, we apply local tracking algorithm to trace crack path.

In the current paper, we seek to extend 2D augmented finite element method (AFEM), which has been proven to be able to account for multiple, arbitrary cracks and crack interactions in solids with much improved numerical efficiency [15–17] to account for 3D crack evolution in solids. The AFEM lies in the category of the embedded discontinuity method without employing discontinuous shape functions.

The remainder of this paper is organized as follows: After a short review of the problem statement and governing equations in Section 2, we briefly discuss the finite element discretization within the frame-work AFEM scheme in Section 3. Section 4 discusses the local crack tracing algorithm used in this study. Then, several numerical examples will be presented as compared with other works in Section 5. Finally, Section 6 concludes the paper with major highlights and numerical achievements.

2. Problem statement

Assume the 3D domain Ω of Fig. 1 is cut by a discontinuity into two sub-domains of Ω^+ and Ω^-. The discontinuity is assumed to be a cohesive crack with interface of $\Gamma_c = \Gamma_c^+ \cup \Gamma_c^-$. For $\Gamma_c^+ = \Gamma_c^-$, the discontinuity is weak and the interface is connected, while for strong discontinuity two surfaces are separated. The $\mathbf{f}$ and $\bar{\mathbf{u}}$ are prescribed traction and displacement on boundary of Γ_f, and Γ_u, respectively. The strong form of equilibrium equations along with boundary conditions are

$$\begin{aligned} &\text{Div}(\boldsymbol{\sigma}^+) = 0 \quad (\forall \mathbf{x} \in \Omega) \qquad \text{Div}(\boldsymbol{\sigma}^-) = 0 \quad (\forall \mathbf{x} \in \Omega^-) \\ &\boldsymbol{\sigma}^+ \cdot \mathbf{n}^+ = \mathbf{f}^+ \quad (\forall \mathbf{x} \in \Gamma_F^+) \qquad \boldsymbol{\sigma}^- \cdot \mathbf{n}^- = \mathbf{f}^- \quad (\forall \mathbf{x} \in \Gamma_F^-) \end{aligned} \quad (1)$$

where $\mathbf{n}^+$ and $\mathbf{n}^-$ are the outward normal of discontinuity surfaces, and $\boldsymbol{\sigma}^+$ and $\boldsymbol{\sigma}^-$ are the stresses in subdomains.

From the stress continuity across the discontinuity boundary, it follows.

$$\begin{aligned} &\mathbf{u}^+ = \bar{\mathbf{u}}^+ \qquad\qquad (\forall \mathbf{x} \in \Gamma_u) \quad \mathbf{u}^- = \bar{\mathbf{u}}^- \qquad\qquad (\forall \mathbf{x} \in \Gamma_u^-) \\ &\mathbf{t}^+ = \boldsymbol{\sigma}^+ \cdot \mathbf{n}^+ = -\mathbf{t} \quad (\forall \mathbf{x} \in \Gamma_c^+) \quad \mathbf{t}^- = \boldsymbol{\sigma}^- \cdot \mathbf{n}^- = \mathbf{t} \quad (\forall \mathbf{x} \in \Gamma_c^-) \end{aligned} \quad (2)$$

where $\mathbf{t}^+$ and $\mathbf{t}^-$ are the tractions along the discontinuity surfaces and $\mathbf{u}^+$ and $\mathbf{u}^-$ are the displacement fields in Ω^+ and Ω^-, respectively.

The traction is a function of the relative displacements ($\mathbf{t} = \mathbf{t}(\Delta\mathbf{u})$) between Γ_c^+ and Γ_c^-, where the relative displacement is $\Delta\mathbf{u} = \mathbf{u}^+ - \mathbf{u}^-$.where $\mathbf{u}^+$ and $\mathbf{u}^-$ are the displacement fields in Ω^+ and Ω^-, respectively. The constitutive law for traction-separation is a piece-wise linear in this study (See Appendix A).

The constitutive law and kinematic equations for subdomain Ω with the assumption of small strain and elastic behavior are written as

$$\begin{aligned} &\boldsymbol{\sigma}^+ = \mathbf{C}^+ : \boldsymbol{\varepsilon}^+ \ (\text{in } \Omega^+) \qquad\qquad \boldsymbol{\sigma}^- = \mathbf{C}^- : \boldsymbol{\varepsilon}^- \ (\text{in } \Omega^-) \\ &\boldsymbol{\varepsilon}^+ = \boldsymbol{\varepsilon}^+(\mathbf{u}^+) = \left[\nabla\mathbf{u}^+ + (\nabla\mathbf{u}^+)^{\mathbf{T}}\right]/2 \ (\text{in } \Omega^+) \\ &\boldsymbol{\varepsilon}^- = \boldsymbol{\varepsilon}^-(\mathbf{u}^-) = \left[\nabla\mathbf{u}^- + (\nabla\mathbf{u}^-)^{\mathbf{T}}\right]/2 \ (\text{in } \Omega^-) \end{aligned} \quad (3)$$

where $\mathbf{C}^+$ and $\mathbf{C}^-$ are the material stiffness tensors of the two sub-domains traversed by the discontinuity, respectively. They are identical for homogeneous materials and different for heterogeneous materials.

The strong form of Eq. (3) can be written into a weak form using the principle of virtual work.

Table 1
Summary of crack tracking methods.

| Tracking method	Remarks
Local method	The crack surface is largely determined by the local elements immediately ahead of a crack front, subjecting to possible constraints from its neighboring crack points and surfaces [7,42,43]. The crack surface is of C^0 continuity, the computational cost is relatively low *Drawback*: The method may have difficulty in modeling non-planar crack
Non-local method	The crack surface is based on a least-squares fit to extend the existing crack surface as smoothly as possible [45,46]. Crack surface has less spurious zick-zack-type crack surfaces *Drawback*: The computational cost of this method is high, the crack surface may deviate from the real path, the complexity of implementation is relatively high.
Global method	An additional equation (heat conduction like) is introduced to track the crack front and provide *iso*-surface for crack [47,48]. The method is computationally robust and the crack surface the outcome of the solution of additional equation *Drawback*: It is computationally expensive due to the extra DoFs from heat conduction equation and requires a judicial choice of an initial boundary condition which is not always obvious for multiple cracking problems or different material interfaces.
Level set method	Signed distance functions is used to describe the crack surfaces [51–53] *Drawback*: There are some issues with freezing the crack surfaces as a crack grows, and inadequacy of finite element mesh for accurately solving the differential equations
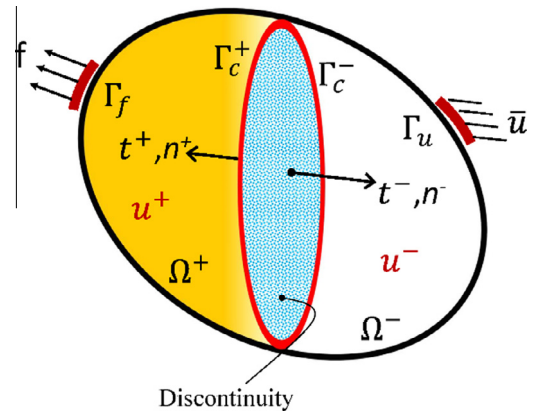
Fig. 1. Elastic body configuration with an arbitrary discontinuity.

$$\begin{aligned} &\int_{\Omega^+} \boldsymbol{\sigma}^+ : \boldsymbol{\varepsilon}^+(\mathbf{u}^+) d\Omega + \int_{\Gamma_c^+} \mathbf{t}(\Delta\mathbf{u}) \cdot \delta(\mathbf{u}^+) d\Gamma = \int_{\Gamma_F^+} \mathbf{f}^+ \cdot \mathbf{u}^+ d\Gamma \qquad \forall \mathbf{u}^+ \in u \\ &\int_{\Omega^-} \boldsymbol{\sigma}^- : \boldsymbol{\varepsilon}^-(\mathbf{u}^-) d\Omega - \int_{\Gamma_c^-} \mathbf{t}(\Delta\mathbf{u}) \cdot \delta(\mathbf{u}^-) d\Gamma = \int_{\Gamma_F^-} \mathbf{f}^- \cdot \mathbf{u}^- d\Gamma \qquad \forall \mathbf{u}^+ \in u \end{aligned} \quad (4)$$

3. AFEM formulation for A 3D 4-node tetrahedron

In this section we describe how to augment a 3D tetrahedron element with only regular nodes and DoFs. More details can be found in the work of Yang and co-workers [15–18]. A 4-node tetrahedron element is chosen to demonstrate the AFEM scheme (Fig. 2). As cut by a cohesive crack, there are two possibilities for tetrahedron cut including a) a tetrahedron sub-domain and a wedge sub-domain (Fig. 2b), b) two wedge sub-domains (Fig. 2c). Regular or external nodes and internal nodes are shown in cut element of Fig. 2. The crack front always resides at element boundaries during its propagation [17,18] and it is also assumed that
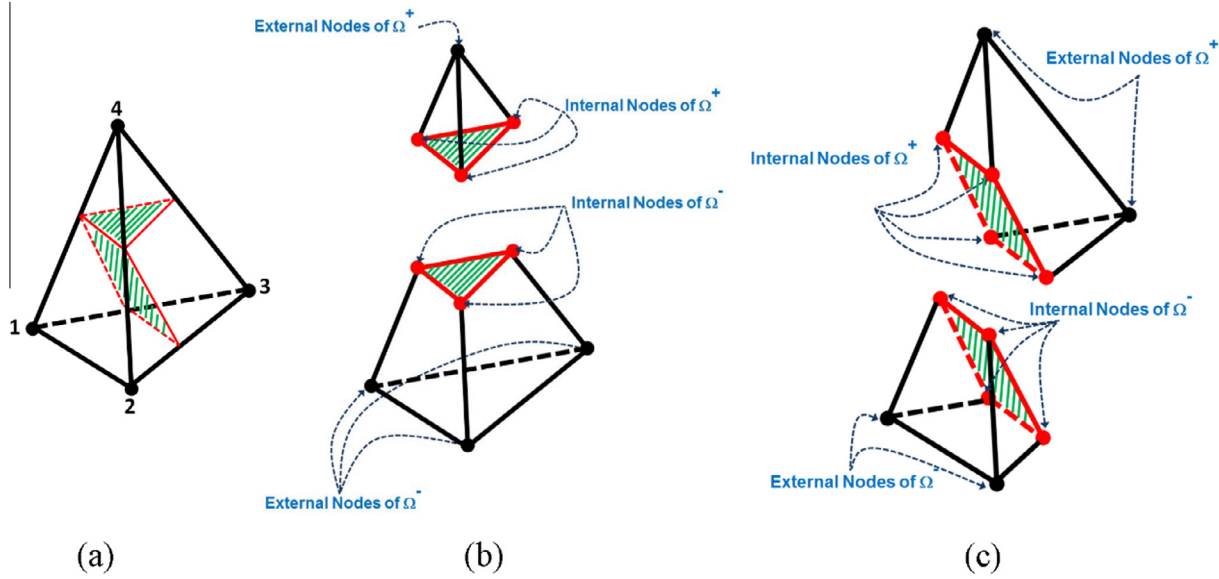
Fig. 2. Schematic of element augmentation for (a) a regular 4-node tetrahedron element with two possible cut, (b) Element cut with tetrahedron and wedge sub-domains, (c) Element cut with two wedge sub-domains.

the existence of a crack front cohesive zone eliminates the crack-tip singularity [3].

Using the principle of virtual work, the weak form of the equilibrium equations for the subdomains shown in Fig. 2 can be written as

$$\begin{cases} \mathbf{L}^+ \cdot \mathbf{d}^+ = \mathbf{F}_{ext}^+ + \mathbf{F}_{int}^+ \\ \mathbf{L}^- \cdot \mathbf{d}^- = \mathbf{F}_{ext}^- + \mathbf{F}_{int}^- \end{cases} \tag{5}$$

where $\mathbf{D}^\alpha$ is the material stiffness matrix of subdomain $\alpha(\alpha = +, -)$. The $\mathbf{L}^\alpha = \int_{\Omega_e^\alpha} (\mathbf{B}^\alpha)^{\mathbf{T}} \mathbf{D}^\alpha \mathbf{B}^\alpha d\Omega$ is the stiffness matrix equivalent to subdomain $\alpha(\alpha = +, -)$, $\mathbf{F}_{ext}^\alpha = \int_{\Gamma_F^\alpha} (\mathbf{N}^\alpha)^{\mathbf{T}} \mathbf{f}^\alpha d\Gamma$ is the equivalent external nodal force on subdomain $\alpha(\alpha = +, -)$ and $\mathbf{F}_{int}^\alpha = \int_{\Gamma_c^\alpha} (\mathbf{N}_{coh}^\alpha)^{\mathbf{T}} \mathbf{t}^a d\Gamma$ is the equivalent internal nodal force obtained from the cohesive stresses along the cohesive crack. $\mathbf{N}_{coh}^\alpha$ is the interpolation matrix of the cohesive crack plane and $\mathbf{B}^\alpha$ represents the strain matrix. Symbols with subscript "ext" and "int" signify quantities at "external" or "internal" nodes in the corresponding subdomains of cut element in Fig. 2. The reader can find more detailed of these definitions in the work of Yang and co-workers [15–18].

It is assumed that while the conformity of the internal DoFs corresponding to the internal nodes ($\mathbf{d}_{int}^+$ and $\mathbf{d}_{int}^-$) is not imposed, the inter-element continuity is enforced only through the external nodal DoFs ($\mathbf{d}_{ext}^+$ and $\mathbf{d}_{ext}^-$) [17,18]. This assumption states that $\mathbf{F}_{ext}^\alpha$ is only a function of external DoFs ($\mathbf{d}_{ext}^+$ and $\mathbf{d}_{ext}^-$) and $\mathbf{F}_{int}^\alpha$ is only a function of internal DoFs ($\mathbf{d}_{int}^+$ and $\mathbf{d}_{int}^-$). Hence, one can rewrite Eq. (5) as

$$\begin{cases} \begin{bmatrix} \mathbf{L}_{11}^+ & \mathbf{L}_{12}^+ \\ \mathbf{L}_{21}^+ & \mathbf{L}_{22}^+ \end{bmatrix} \begin{Bmatrix} \mathbf{d}_{ext}^+ \\ \mathbf{d}_{int}^+ \end{Bmatrix} = \begin{Bmatrix} \mathbf{F}_{ext}^+ \\ \mathbf{F}_{int}^+ \end{Bmatrix} \\ \begin{bmatrix} \mathbf{L}_{11}^- & \mathbf{L}_{12}^- \\ \mathbf{L}_{21}^- & \mathbf{L}_{22}^- \end{bmatrix} \begin{Bmatrix} \mathbf{d}_{ext}^- \\ \mathbf{d}_{int}^- \end{Bmatrix} = \begin{Bmatrix} \mathbf{F}_{ext}^- \\ \mathbf{F}_{int}^- \end{Bmatrix} \end{cases} \tag{6}$$

where $\mathbf{L}_{ij}^\alpha$ (i, j = 1, 2) are the sub-matrices of stiffness matrix $\mathbf{L}^\alpha$, i.e., $\mathbf{L}^\alpha = \begin{bmatrix} \mathbf{L}_{11}^\alpha & \mathbf{L}_{12}^\alpha \\ \mathbf{L}_{21}^\alpha & \mathbf{L}_{22}^\alpha \end{bmatrix}$. It is noted that $\mathbf{L}_{11}^\alpha$ and $\mathbf{L}_{22}^\alpha$ are the sub-stiffness matrix related to the external and internal nodes of the subdomain α, respectively. Using stress continuity across the cohesive crack

plane, internal nodal forces at subdomains are linked as $\mathbf{F}_{int}^- = -\mathbf{F}_{int}^+ = \int_{\Gamma_c} (\mathbf{N}_{coh})^{\mathbf{T}} \mathbf{t} d\Gamma$.

The displacements of internal nodes are obtained following the same procedure explained in Refs. [17,18] as

$$\begin{Bmatrix} \mathbf{d}_{int}^+ \\ \mathbf{d}_{int}^- \end{Bmatrix} = \begin{bmatrix} -\mathbf{A}^{-1} \cdot (\mathbf{I} - \boldsymbol{\alpha} \cdot (\boldsymbol{\Psi}_{22}^-)^{-1}) & 0 \\ 0 & \mathbf{B}^{-1} \cdot (\mathbf{I} - \boldsymbol{\alpha} \cdot (\boldsymbol{\Psi}_{22}^+)^{-1}) \end{bmatrix} \begin{Bmatrix} \mathbf{S_0} \\ \mathbf{S_0} \end{Bmatrix}$$
$$+ \begin{bmatrix} -\mathbf{A}^{-1} \cdot \boldsymbol{\alpha} \cdot (\boldsymbol{\Psi}_{22}^-)^{-1} \cdot \mathbf{L}_{21}^- & -\mathbf{A}^{-1} \cdot \mathbf{L}_{21}^+ \\ -\mathbf{B}^{-1} \cdot \mathbf{L}_{21}^- & -\mathbf{B}^{-1} \cdot \boldsymbol{\alpha} \cdot (\boldsymbol{\Psi}_{22}^+)^{-1} \cdot \mathbf{L}_{21}^+ \end{bmatrix} \begin{Bmatrix} \mathbf{d}_{ext}^- \\ \mathbf{d}_{ext}^+ \end{Bmatrix} \tag{7}$$

where

$$\mathbf{S_0} = A_e \mathbf{R}^{\mathbf{T}} \cdot \mathbf{T}_{coh} \cdot \boldsymbol{\sigma}_0; \boldsymbol{\alpha} = A_e \mathbf{R}^{\mathbf{T}} \cdot \mathbf{T}_{coh} \cdot \boldsymbol{\alpha}_0 \cdot \mathbf{N}_{coh} \cdot \mathbf{R}; \boldsymbol{\Psi}_{22}^+ = \mathbf{L}_{22}^+ + \boldsymbol{\alpha}; \boldsymbol{\Psi}_{22}^- = \mathbf{L}_{22}^- + \boldsymbol{\alpha}$$

$$\mathbf{A} = \boldsymbol{\Psi}_{22}^+ - \boldsymbol{\alpha} \cdot (\boldsymbol{\Psi}_{22}^-)^{-1} \cdot \boldsymbol{\alpha}; \mathbf{B} = \boldsymbol{\Psi}_{22}^- - \boldsymbol{\alpha} \cdot (\boldsymbol{\Psi}_{22}^+)^{-1} \cdot \boldsymbol{\alpha}$$

$$\boldsymbol{\sigma}_0 = \{ \mathrm{sgn}(\delta_{sA})(\hat{\tau}_{sA}^{(i-1)} - \alpha_{sA}^{(i)} \delta_{sA}^{(i-1)}),$$

$$\mathrm{sgn}(\delta_{tA})(\hat{\tau}_{tA}^{(j-1)} - \alpha_{tA}^{(j)} \delta_{tA}^{(j-1)}), (\hat{\sigma}_A^{(k-1)} - \alpha_{nA}^{(k)} \delta_{nA}^{(k-1)}), \ldots \}^{\mathbf{T}}$$

$$\boldsymbol{\alpha}_0 = \mathrm{Diag}[\alpha_{sA}^{(i)}; \alpha_{tA}^{(j)}; \alpha_{nA}^{(k)}; \alpha_{sB}^{(l)}; \alpha_{tB}^{(m)}; \alpha_{nB}^{(n)}; \ldots]$$

and $\mathbf{I}$ is the identity matrix, $\mathbf{R}$ represents the rotation matrix and A_e is the crack surface area. $\mathbf{T}_{coh}$ signifies the respective integration matrix associated with the cohesive stress integration. $\boldsymbol{\sigma}_0$ and $\boldsymbol{\alpha}_0$ are cohesive stress and slope of cohesive segment (See Appendix A), respectively.

The relationship between cohesive stresses and the local cohesive displacements at any point on the crack plane is given in Appendix A. It is noted that a three-point (A, B, C) integration scheme reported in [55] is chosen for the tetrahedron-wedge cut configuration (Fig. 2b) for triangular crack plane, while a standard 4-point Gaussian quadrature (A, B, C, and D) with iso-parametric mapping is used for the wedge-wedge cut configuration and quadrilateral crack plane (Fig. 2c).

Due to non-linear nature of Eq. (7), a consistency-check based solving algorithm developed by Yang and colleagues [15–18] is employed for solving Eq. (7). In this method the internal nodal displacements (Eq. (7)) is solved analytically through a simple consistency checking procedure instead of solving the incremental form of the elemental equilibrium. The detailed consistency-check based algorithm is reported in [17,18].

Once a solution is guaranteed from Eq. (7), submatrices of Eq. (6) are defined. Then, by eliminating internal displacements from Eq. (6), fully condensed equilibrium equation without any internal forces and displacement can be obtained as follows [17,18]

$$
\left\{ \begin{array}{c} \mathbf{F}_{ext}^- \\ \mathbf{F}_{ext}^+ \end{array} \right\} = \left[\begin{array}{cc} \mathbf{L}_{11}^- - \mathbf{L}_{12}^- \cdot \mathbf{B}^{-1} \cdot \mathbf{L}_{21}^- & -\mathbf{L}_{12}^- \cdot \mathbf{B}^{-1} \cdot \boldsymbol{\alpha} \cdot (\boldsymbol{\Psi}_{22}^+)^{-1} \cdot \mathbf{L}_{21}^+ \\ -\mathbf{L}_{12}^+ \cdot \mathbf{A}^{-1} \cdot \boldsymbol{\alpha} \cdot (\boldsymbol{\Psi}_{22}^-)^{-1} \cdot \mathbf{L}_{21}^- & \mathbf{L}_{11}^+ - \mathbf{L}_{12}^+ \cdot \mathbf{A}^{-1} \cdot \mathbf{L}_{21}^+ \end{array} \right] \left\{ \begin{array}{c} \mathbf{d}_{ext}^- \\ \mathbf{d}_{ext}^+ \end{array} \right\}
$$
$$
- \left[\begin{array}{cc} \mathbf{L}_{12}^- \cdot \mathbf{B}^{-1} \cdot \left[\mathbf{I} - \boldsymbol{\alpha} \cdot (\boldsymbol{\Psi}_{22}^+)^{-1} \right] & 0 \\ 0 & -\mathbf{L}_{12}^+ \cdot \mathbf{A}^{-1} \cdot \left[\mathbf{I} - \boldsymbol{\alpha} \cdot (\boldsymbol{\Psi}_{22}^-)^{-1} \right] \end{array} \right] \left\{ \begin{array}{c} \mathbf{S_0} \\ \mathbf{S_0} \end{array} \right\}
$$
(8)

4. Crack tracking

One of the important essentials in three dimensional crack propagation is the determination of normal of the crack plane. The literature contains noteworthy works related to crack tracing schemes with their on advantages and drawbacks [39–54]. We employ a local tracking algorithm with maximum principle stress direction as criterion for normal of crack plane. Crack propagation starts if crack tip stress exceeds the cohesive strength. Different possibilities in which an element can be traversed by a crack is shown in Fig. 3a. Element with one existing crack is possibly has triangle or quadrilateral crack plane. In this case, the crack plane normal must be calculated ensuring the crack surface continuity between the existing crack and the new crack plane. The crack plane of an element with more than one crack edge is fully known.

For the case with one existing crack, we applied special treatment to maintain crack continuity. It should be noted that crack plane determined by maximum principle stress direction in the current element may not have the existing crack front. To maintain the crack continuity, a local coordinate system $(\mathbf{e}_1, \mathbf{e}_2, \mathbf{e}_3)$ is defined on the existing crack edge (Fig. 3b) with $\mathbf{e}_3$ perpendicular to the plane of the neighbor element fully cut by crack; $\mathbf{e}_2$ along the crack front (e.g. Y' in Fig. 3b); and $\mathbf{e}_1 = \mathbf{e}_2 \times \mathbf{e}_3$. The continuity between the existing and new crack plane dictates that the out-normal direction of the new crack plane must be in parallel with the plane spanned by $\mathbf{e}_1$ and $\mathbf{e}_3$ ($X' - Y'$ plane). If the principle stress direction in the current element is not parallel with the $X' - Y'$ plane, we simply project principle stress onto the $X' - Y'$ plane and use the projected direction as the out-normal of the new crack plane, as shown in Fig. 3b. This is totally local treatment guaranteeing C^0 continuity of the crack plane across elements.

It is noted that a numerical treatment in the crack tracking algorithm is considered to avoid a potential crack plane cutting directly into an elemental node. If that situation takes place, the volume of one of the subdomains becomes zero, causing severe difficulty in numerical convergence. In this work, once this condition is detected, the crack plane is slightly rotated about the crack front line. The rotation maintains vertical distance between modified crack plane and the node 1/20th of the smallest edge length of the element.

5. Numerical examples and discussions

In this section, the 3D AFEM is applied to four examples to investigate its numerical performance. The AFEM method is implemented into user-defined element (UEL) of commercial FE package ABAQUS. The presented computations are performed on a Dell precision T1700 ($\times$64 bit) mobile workstation with Intel Core i7–4790 CPU @ 3.6 GHz and with 32 GB of RAM. The considered examples are the simulation of a single-edge notch beam, a double-notched shear beam, fiber/matrix interface debonding and kinking and open hole tension of a cross-ply laminate.

5.1. Single-edge-notched beam test

A single-edge-notched beam is subjected to bending loading as presented in Fig. 4. According to the experimental tests reported in [56,57], two different geometries are modeled including model D1 with the width of $D = 75$ mm, and model D2 with the width of $D = 150$ mm. Two different types of each model are considered for fracture analysis using AFEM. In the first type (Type I), the top left of the beam is free to move vertically without any restriction (Fig. 4a), while in the second type, the vertical movement of the top left of the beam is prevented (Fig. 4b). In both cases, the beam is simply supported at the bottom and loaded downward by a displacement-controlled loading at the top. The notch depth is 0.5D, except for Type 2 of the small model (Model D1), it is 0.6D. The material properties are: Young's modulus E = 38 Gpa, Poisson's ratio $v = 0.18$, cohesive strength of 3 Mpa, and fracture toughness of 69 N/m [56].

Two different meshes are analyzed in each model including 5874 and 8422 tetrahedron elements for model D1, and 6238 and 9052 tetrahedron elements for model D2. The mesh sizes are considerably smaller than the cohesive zone size or fracture process zone size, which according to the order-of-magnitude estimation $l_{coh} = \Gamma_{Ic}E/2\hat{\sigma}^2$, is about $l_{coh} = 145$ mm. To compare with experimental data, the crack initiation location is set to be on the bottom surface where the notch is located. The procedure of crack initiation and propagation from the initiation spot is automatically
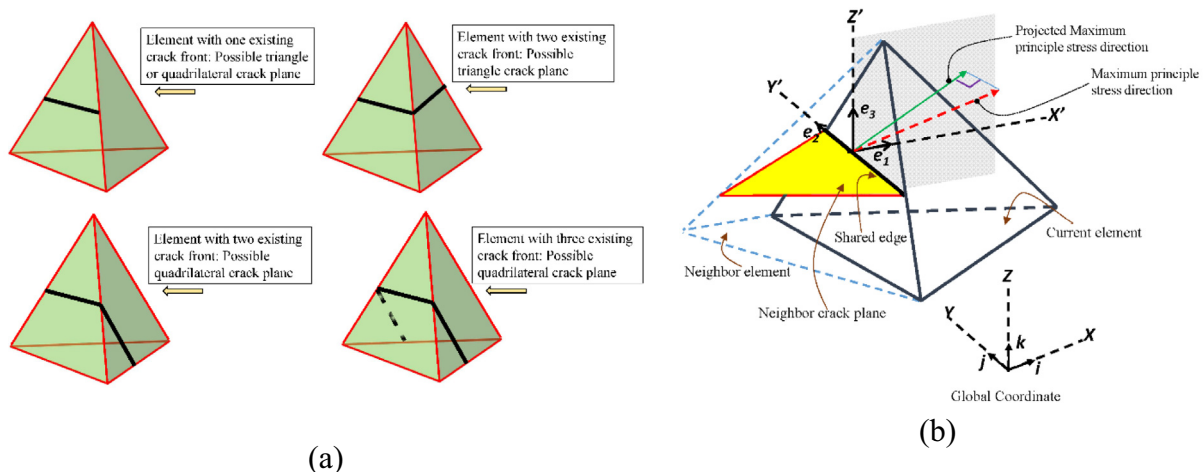

Fig. 3. a) Schematic of possible element cut by crack plane, b) Illustration of crack propagation scheme.
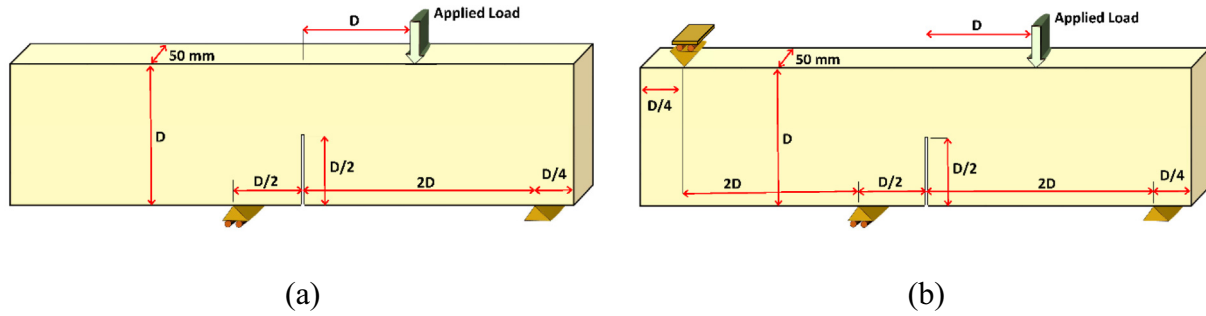
Fig. 4. Schematic drawing of single-edge-notch beam a) Type I: The left top is free to move vertically; b) Type II: vertical displacement of top left is restricted.
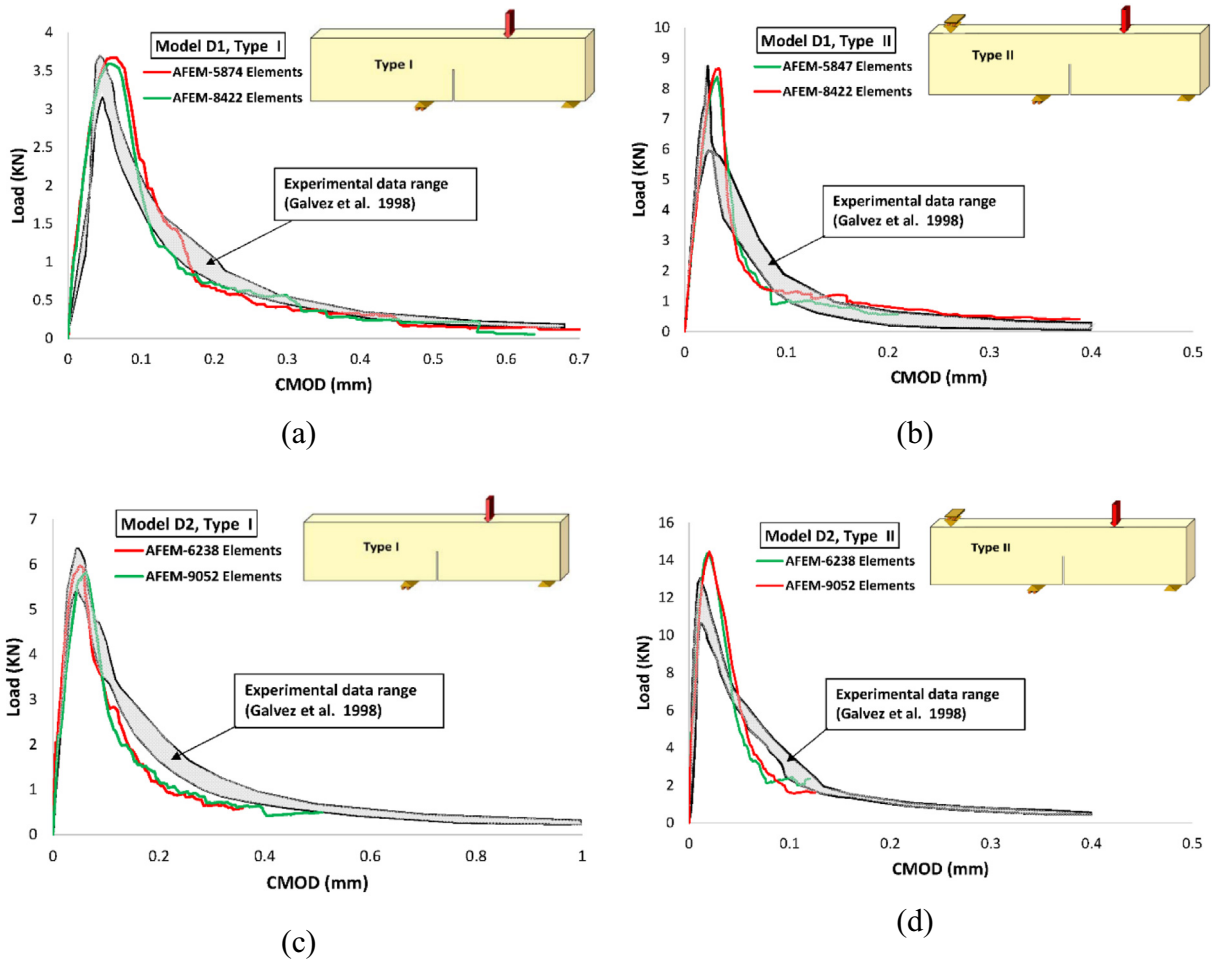

Fig. 5. Comparison of numerical reaction force versus CMOD with experimental test data reported by Galvez et al. 2001 [56], a) Model D1 with D = 75 mm, Type I; b) Model D1 with D = 75 mm, Type II; Model D2 with D = 150 mm, Type I; c) Model D2 with D = 150 mm, Type II.

determined by maximum principle criterion. Load versus crack mouth opening displacement (CMOD) and crack path trajectories are compared with the test data reported in Ref. [56].

Fig. 5(a-b) compares the 3D AFEM simulated load vs. CMOD curves with the test results obtained by Galvez et al. [56] for Model D1 (D = 75 mm), Type I and II with two different mesh sizes. The 3D AFEM load-displacement curves obtained with the two meshes are all consistent with the test data and they are in fair agreement with test results. As presented in Fig. 5(c-d), the results are pertained to Model D2 (D = 150 mm), Type I and II for two different mesh sizes. Although the peak loads are underestimated or overes-

timated by about 10% for large model (Model D2), the overall characteristics of the curve remain consistent with test data. Also, in numerical predictions of large model, the load-CMOD curve is slightly descending faster than that of test data. As pointed out in Ref. [56], the reason may be related to the fact that the fracture energy of mixed mode in large specimen is higher in small specimen.

Fig. 6a–b shows the experimental envelope and the numerical prediction of the crack paths for the two different models. The numerical crack path are consistent with the experimental recorded crack envelope.
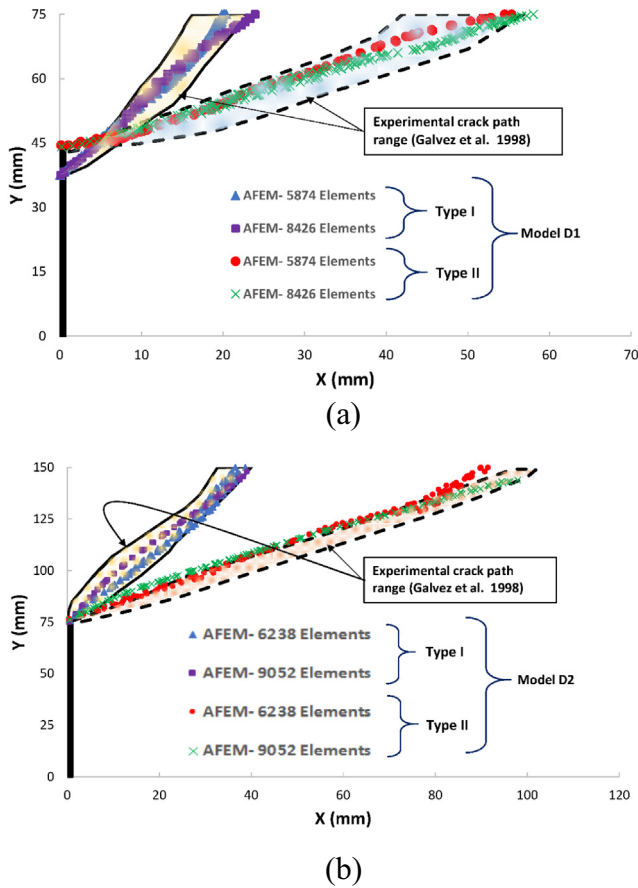

Fig. 6. Comparison of numerical crack path with experimental crack path reported by Galvez et al. 2001 [56], a) Model D1 with D = 75 mm, Type I; b) Model D1 with D = 75 mm, Type II; Model D2 with D = 150 mm, Type I; c) Model D2 with D = 150 mm, Type II.

5.2. Double-notched shear beam test

In this numerical example, the crack propagation process in a double-notched four point shear beam specimen reported Bocca et al. [58] is simulated. The geometry, boundary conditions and loading of the double-notched beam are shown in Fig. 7a. Material properties are $E = 27$ GPa; $v = 0.1$, fracture energy of $\Gamma_{Ic} = \Gamma_{IIc} = 100$ N/mm and cohesive strength of $\hat{\sigma} = 2$ Mpa. The mesh sizes are noticeably smaller than the cohesive zone size or fracture process zone size, which according to the order-of-magnitude estimation $l_{coh} = \Gamma_{Ic}E/2\hat{\sigma}^2$, is about $l_{coh} = 335$ mm roughly twice the beam height. To compare with experimental data, the crack initiation location is set to be on the bottom surface where the two notches is are located. Initiation and propagation of the cracks are totally automatic in the 3D AFEM obtained by stress criterion.

This example is well-known to mixed mode fracture of brittle material with instability in load-deflection curve. A snap-back behavior in the load-deflection curve results in global instability and difficulty in numerical convergence. The snap-back behavior is linked to the material properties and dimension of the specimen. Usually for large specimen and small fracture toughness, instability and snap-back is imminent. The arc-length method available in the ABAQUS simulation package is used to capture this behavior. The beam is discretized into two different meshes with 5680 and 9407 tetrahedron elements.

Fig. 7b shows the simulated load-displacement responses as compared with test data and numerical simulation reported in Ref. [58]. The current simulation results are comparable with the
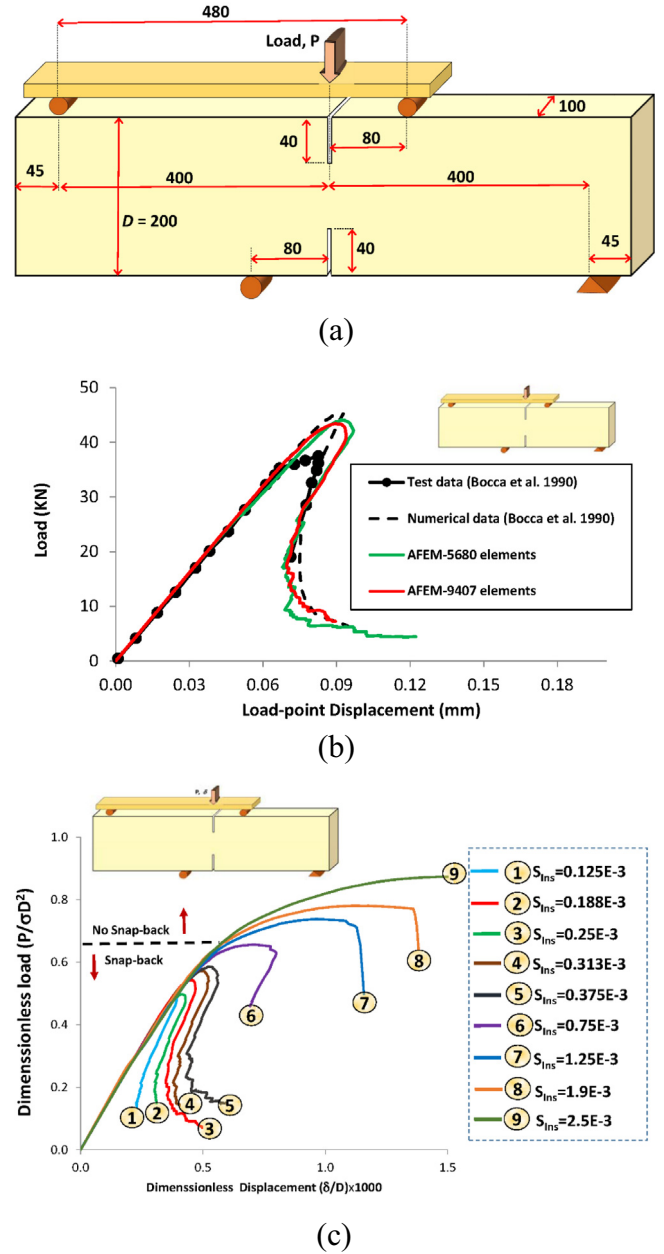

Fig. 7. a) Schematic drawing of doubled-edge-notched beam under four point shear test (All dimensions in mm); b) Comparison of three-dimensional AFEM simulated load-displacement curve with experimental data and numerical results of Ref. [58], c) Size effect and instability analysis.

numerical results reported in Ref. [58]. However, except for the peak load magnitude, the numerical results of pre-peak and post peak snap-back are qualitativly in fair agreement with test data. The predicted peak loads in both 3D AFEM and numerical reuslts of Ref. [58] are higher than the experimental peak load. This could be due to the fact that the assumed fracture toughness is at the higher bound for concretes and the mode I fracture energy is usually different from the mode II fracture energy.

In addition to load–displacement curve, an instability analysis is numerically performed to study the fracture of material with snap-back response. According to Bocca's work [58], an instability parameter is defined as $S_{Ins} = \Gamma_{Ic}/\hat{\sigma}D$ with D as the width of the model. The results are presented in Fig. 7c. In this figure the ordinate corresponds to a dimensionless load defined as $P/\hat{\sigma}D^2$, while the abscissa is the dimensionless deflection defined as δ/D with δ
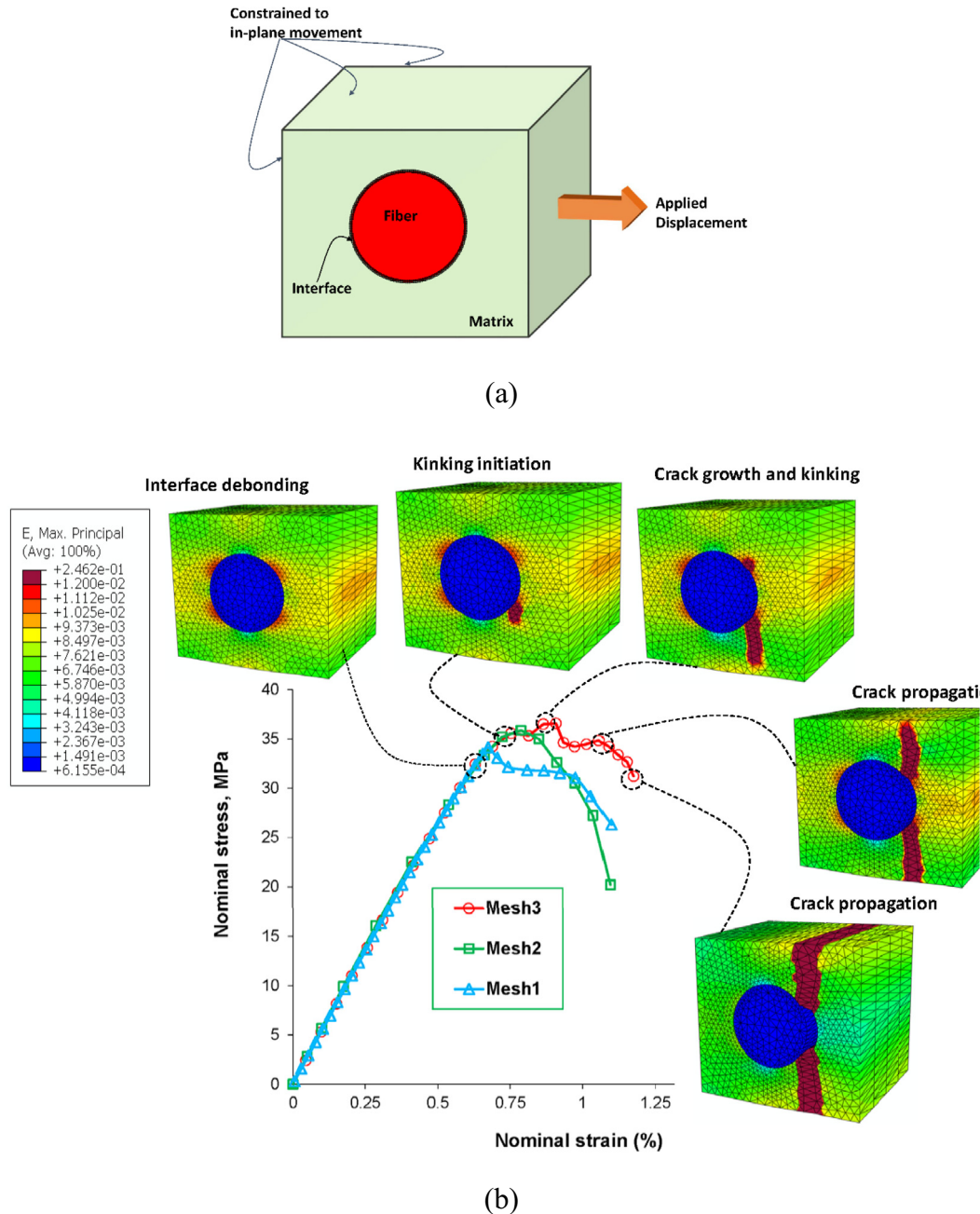
(a)

(b)

Fig. 8. a) Schematic drawing of single fiber/matrix model along with boundary conditions, b) 3D AFEM simulate nominal stress versus nominal strain for three different meshes (Mesh1: 4650 elements; Mesh2: 11111 elements; Mesh3: 27094 elements) along with contour plot of debonding, crack initiation and propagation for Mesh3.

as deflection of load point. The results of Fig. 7c are obtained by changing the fracture toughness in the instability parameter (S_{Ins}). It is seen that as instability parameter increases, the snap back effect reduces and more stable crack propagation is expected. The figure also reveals that for instability parameter roughly greater than $S_{Ins} \approx > 7.5 \times 10^{-4}$, the snap-back is not probable. The current results are consistent with instability region reported by Bocca et al. [58].

5.3. Coupled fiber–matrix interface debonding and kinking

In this numerical example, the capability of 3D AFEM is demonstrated by single fiber–matrix debonding and kinking. As shown in Fig. 8, a cube of 1 mm × 1 mm × 1 mm with a fiber of 0.5 mm in diameter in the center is considered for debonding and kinking

example. The fiber volume fraction is 19.63%. Boundary conditions are shown in Fig. 8a. Three different mesh sizes are considered to simulate the problem including Mesh1 = 4650, Mesh2 = 11111, and Mesh3 = 27094. The Young modulus and Poisson's ratio for fiber are $E = 40$ Gpa and $v = 0.33$, respectively. And, for matrix, Young modulus and Poisson's ratio are $E = 4$ Gpa and $v = 0.4$, respectively. The cohesive strength and fracture energy for matrix are 50 Mpa and 250 N/m, respectively. The process of crack initiation and kinking is automatic in the model. Since it is not possible to display UEL results in ABAQUS viewer, to visualize the user element output (strains) in ABAQUS viewer, a dummy overlaid mesh with very small Young's modulus (10^{-15}) is defined.

To account for interfacial debonding, zero thickness cohesive elements are inserted between matrix and fiber. However the linear triangular traction-separation cohesive law is very common
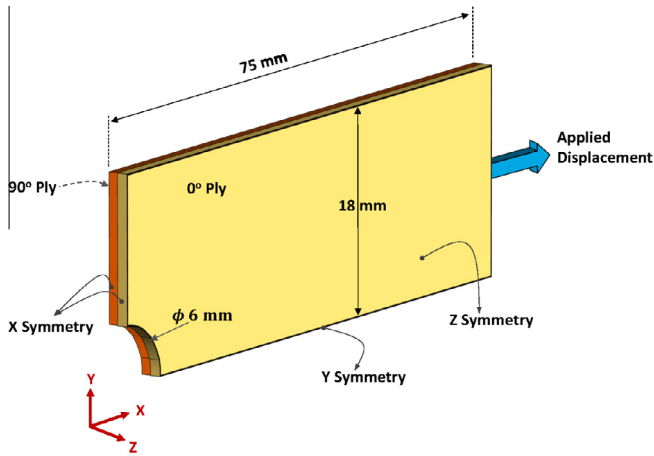
Fig. 9. Schematic drawing of open-hole tension model with specified boundary conditions.

Table 2
Material properties for HTA/6376 carbon/epoxy [62,64].

E_{11} (Gpa)	$E_{22} = E_{33}$ (Gpa)	$G_{12} = G_{13}$ (Gpa)	G_{23} (Gpa)	$v_{12} = v_{13}$	v_{23}
139	10	5.2	3.48	0.3	0.51
G_{Ic} (N/m)	G_{IIc} (N/m)	$\hat{\sigma}_n$ (Mpa)	$\hat{\tau}_s = \hat{\tau}_t$ (Mpa)		
260	1002	30	60		

and simple to be implemented for debonding, in this work, for better consistency and accuracy of capturing debonding, the potential based cohesive law of Paulino and co-workers [59,60] is used. Appendix B gives a summary of this method. It is out of the scope of the current work to discuss about potential based cohesive laws and the details are refereed to Paulino' work [59,60].

Once debonding starts at the interface, crack is initiated at the most critical matrix element close to interface with maximum local stress. In order to impose debonding earlier than matrix cracking, the interfacial strength of the interface elements (roughly 30 Mpa) are assumed smaller than cohesive strength of matrix. This assumption is in accordance with 2D AFEM numerical work of Liu et al. [16,17] which the debonding initiates around 30 Mpa of nominal stress.

The simulated nominal stress versus strain is plotted in Fig. 8b along with contour of maximum principle strain for different stages of loading. Roughly around nominal strain of 0.7%, the interface is debonded and shortly followed by kinking cracks at 0.75% strain. For the coarse mesh, cracks propagate quickly with drop-off in stress–strain curve. However, for two other finer mesh, cracks gradually propagates followed by a nonlinear response of the material till about 0.8% of nominal strain. With further increasing the load, more cracks developed and composite response starts to drop off. It is seen that for all meshes, the predicted composite modulus is approximately 5.2 Gpa with 7% difference with the composite elastic modulus obtained from lower-bound estimation (4.86 Gpa). Despite the difference among meshes, the composite response is qualitatively is similar. Quantitatively, the results of simulated composite elastic modulus is in a reasonably agreement with lower-bound based modulus. We need to emphasis that the crack processing (initiation and propagation, location of kinking) are calculated by the program according to local stress criterion. In each increment, for those elements whose maximum principle stress exceeds the cohesive strength, the program searches the element with maximum crack initiation index (ratio of maximum

principle stress to the cohesive strength). Once the element with maximum crack initiation index is detected, a crack cuts that element. Also, when one crack is initiated, the balance of failure conditions at other location is changed. Therefore, it is expected that the crack initiation and propagation is not symmetric.

5.4. Open hole tension of a cross-ply laminate

In this section, fracture and multiple cracking of an open hole cross ply carbon fiber epoxy laminate HTA/6376 ($[90_2/0_2]_s$) subjected to static tensile loading is simulated with AFEM. Transverse and splitting cracks are modeled using 3D AFEM within plies. As presented in Fig. 9, due to symmetry, only a quarter of the specimen is molded with symmetric boundary conditions. In the model, only two plies with the thickness of 0.25 mm for each direction is considered because there are two plies of 0° or 90° stacked together. To account for delamination, zero thickness cohesive elements are inserted in fiber/ matrix interface. The model is meshed with 15967 tetrahedron elements with mesh size of roughly 0.25 mm around hole which is an adequate mesh size for the laminate material. The material properties of HTA/6376 is summarized in Table 2 [62–64]. For fiber directions of 0° ply, once the fiber direction strain reaches the failure strain (ε_f = 1.5% [62]), elastic modulus E_{11} is reduced to small value indicating fiber failure. The interface strength is reduced by factor 2 for better convergence in the simulation as suggested Ref. [65,66]. Similar to Fang et al. [67] work, splitting and transverse direction cracks initiate if quadratic criterion of Eq. (9) is satisfied. Transverse and splitting cracks then follows the fiber direction as the propagation direction.

$$\left(\frac{\sigma_{yy}}{\hat{\sigma}}\right)^2 + \left(\frac{\tau_{xy}}{\hat{\tau}_s}\right)^2 + \left(\frac{\tau_{xz}}{\hat{\tau}_t}\right)^2 \geqslant 1 \qquad (9)$$

where σ_{yy} is transverse normal tensile stress, and τ_{12} and τ_{13} are shear stresses in XY and XZ plane, respectively.

It is noted that the location of transverse intra-ply and splitting cracks are automatically determined by the program according to elemental local stresses. The only constrain is that the spacing between matrix cracks is enough to make sure each element and its nodes support one crack (here 0.6 mm for meshes around the hole with ~0.25 mm sizes.

The plot of laminate stress–strain response is presented in Fig. 10a along with test data reported in Ref. [62]. The strain data in this figure are related to the location of ~12 mm away from the center of the hole. The simulation results with arbitrary cracking reasonably correlates with test data. Although the damping factor and implicit dynamic options offered in ABAQUS are used for better convergence, simulation runs up to about 80% of final loading when the program cannot converge due to excessive damage of fiber failure and rise-up of matrix cracks. It is noted that a well-designed, robust and efficient numerical algorithm is needed to handle complex damage including transverse cracks, interface delamination and fiber rupture.
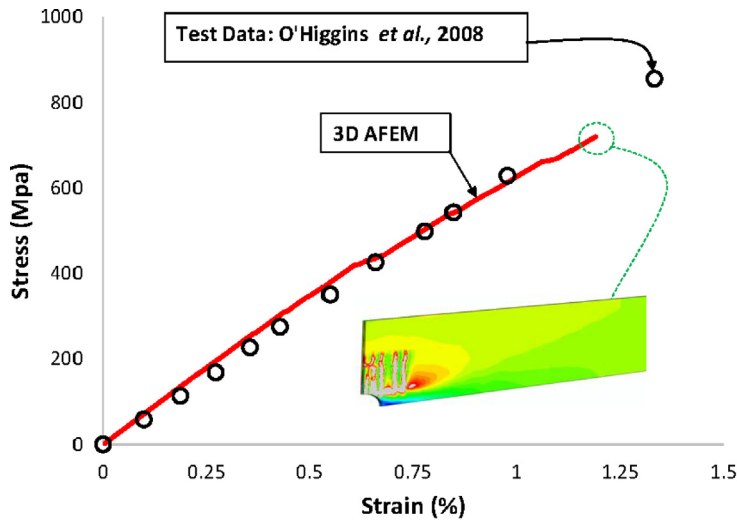
The predicted crack evolution at different laminate load level of 40%, 60%, and 80% is shown in Fig. 10b (white dashed line as splitting and transverse cracks). The contour plot of Fig. 10 is pertained to maximum principle strain. According to simulated results, first crack occurs in 0° ply as the splitting crack at the load level of roughly 35% of final loading and propagates along the fiber direction. Around 40% of loading splitting and two transverse cracks initiate at different locations. As the applied load is increased to ~ 60% of loading, the splitting and more transverse cracks initiate and propagate in the laminate. Also, delamination area (marked as yellow area in Fig. 10b) grows along with other damages. At the 80% of final load level, splitting crack, transverse cracks, and delamination significantly propagate along the fiber directions.

6. Conclusions

In the current paper, arbitrary cracking in solids is simulated by 3D AFEM without the need for additional DoFs. The formulation is implemented into UEL subroutine of ABAQUS with a 4-node tetrahedron element. The 3D AFEM introduces internal node-pairs with normal displacements as internal nodal DoFs. The internal node-pairs are ultimately condensed at elemental level using a consistency-check based condensation algorithm. Hence, the crack displacements are natural results of the elemental equilibrium. The crack surface evolution is computed and recorded using a local tracking technique. Within several numerical examples, the capabilities of 3D AFEM is demonstrated.

Particularly, the global instability (snap-back) numerical example (double notch shear beam) and cracking in cross ply composite laminate show the effectiveness of AFEM. Also, it should be mentioned that augmentation procedure can be extended to other types of 3D elements.

Although the formulation presented in this work is specific to the tetrahedron element cut by a single cohesive crack, there is no technical difficulties to extend the augmentation procedure to multiple cracking and interactive cracking, given the successful implementation and demonstration reported in the 2D AFEM [17]. Finally, multiple cracking and interactive cracking are recommended to be explored within AFEM as well as robust and rigorous numerical algorithm handling numerical convergence issues in

(a)
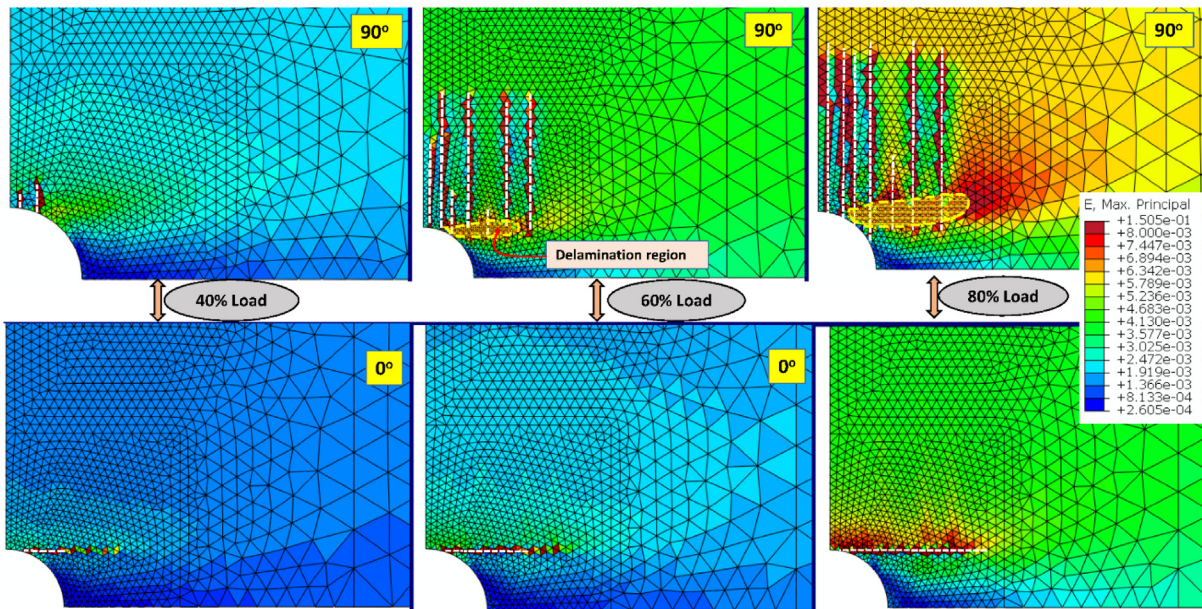
(b)

Fig. 10. a) Predicted stress–strain curve with test data of Ref. [62]; b) AFEM predicted crack evolution at different load level of 40%, 60% and 80% of final loading. Dashed lines are splitting and transverse cracking while the yellow region is delamination area. (For interpretation of the references to color in this figure legend, the reader is referred to the web version of this article.)

composite laminate with networks of complex matrix cracks and debonding.

Acknowledgment

The authors are grateful to Dr. Qingda Yang of University of Miami for his advice and help with augmented finite element method (AFEM).

Appendix A

A.1. Linear constitutive law for cohesive interface

In the current work, as presented in Fig. A1, we employed a mixed-mode linear traction-separation cohesive law. Parameters δ_{nc}, δ_{tc} and δ_{sc} are the critical normal and two shear crack displacements under pure modes beyond which the complete fracture takes place. The $\hat{\sigma}, \hat{\tau}_s$ and $\hat{\tau}_t$ are cohesive normal and shear strength for mode-I, mode-II, and mode III traction-separation laws. Also, δ_{n1}, δ_{s1} and δ_{t1} are crack initiation displacements where softening starts. The superscripts i, j and k are free indices denoting the linear segment number in the respective traction-separation laws

Cohesive stresses are related to cohesive strength, critical and initial displacements as follows [17,18]

$$
\begin{Bmatrix} \tau_s^{(i)} \\ \tau_t^{(j)} \\ \sigma^{(k)} \end{Bmatrix} = \begin{Bmatrix} \mathrm{sgn}(\delta_s)\left(\hat{\tau}_s^{(i-1)} - \alpha_s^{(i)}\delta_s^{(i-1)}\right) \\ \mathrm{sgn}(\delta_t)\left(\hat{\tau}_t^{(j-1)} - \alpha_t^{(j)}\delta_t^{(j-1)}\right) \\ \hat{\sigma}^{(k-1)} - \alpha_n^{(k)}\delta_n^{(k-1)} \end{Bmatrix}
$$
$$
+ \begin{bmatrix} \alpha_s^{(i)} & 0 & 0 \\ 0 & \alpha_t^{(j)} & 0 \\ 0 & 0 & \alpha_n^{(k)} \end{bmatrix} \begin{Bmatrix} \delta_s \\ \delta_t \\ \delta_n \end{Bmatrix} (i, j, k = 1, 2, 3) \tag{A1}
$$

where the slopes of the cohesive segments $\alpha_s^{(i)}, \alpha_t^{(j)}$ and $\alpha_n^{(k)}$ is given by

$$
\begin{aligned}
\alpha_s^{(i)} &= \left(\hat{\tau}_s^{(i)} - \hat{\tau}_s^{(i-1)}\right) / \left(\delta_s^{(i)} - \delta_s^{(i-1)}\right) \\
\alpha_t^{(j)} &= \left(\hat{\tau}_t^{(j)} - \hat{\tau}_t^{(j-1)}\right) / \left(\delta_t^{(j)} - \delta_t^{(j-1)}\right) \\
\alpha_n^{(k)} &= \left(\hat{\sigma}^{(k)} - \hat{\sigma}^{(k-1)}\right) / \left(\delta_n^{(k)} - \delta_n^{(k-1)}\right)
\end{aligned} \tag{A2}
$$

where $\hat{\sigma}^{(0)} = \hat{\tau}_t^{(0)} = \hat{\tau}_s^{(0)} = 0$ and $\delta_n^{(0)} = \delta_t^{(0)} = \delta_s^{(0)} = 0$.

Total traction-separation work absorbed during fracture consists of the work of mode I, work of mode II (G_{II}) and the work of Mode 3 (G_{III}). Total fracture energy can be expressed,

$$
G = G_I(\delta_n) + G_{II}(\delta_s) + G_{III}(\delta_t) \tag{A3}
$$

It is noted that the fracture energy of each mode is the area under traction-separation law. A fracture energy-based failure criteria can be written as [18]

$$
G_I(\delta_{nc})/\Gamma_{IC} + G_{II}(\delta_{sc})/\Gamma_{IIC} + G_{III}(\delta_{tc})/\Gamma_{IIIC} = 1 \tag{A4}
$$

where Γ_{IC}, Γ_{IIC} and Γ_{IIIC} are fracture energy at failure under the pure opening and pure shear traction-separation laws the linear-elastic-fracture mechanics(LEFM) context. The reader is referred to [17,18] for more details.

Appendix B

B.1. A potential based cohesive model

The interfacial debonding of fiber/matrix in the current work is simulated using potential based cohesive law by Paulino and coworkers [59–61]. Following the same notation of Refs. [59–61], the potential energy of cohesive zone is as follows

$$
\Psi(\Delta_n, \Delta_t) = \min(\phi_n, \phi_t) + \left[\Gamma_n\left(1 - \frac{\Delta_n}{\delta_n}\right)^\alpha \left(\frac{m}{\alpha} + \frac{\Delta_n}{\delta_n}\right)^m + \langle\phi_n - \phi_t\rangle\right]
$$
$$
\times \left[\Gamma_t\left(1 - |\frac{\Delta_t}{\delta_t}|\right)^\beta \left(\frac{n}{\beta} + |\frac{\Delta_t}{\delta_t}|\right)^n + \langle\phi_t - \phi_n\rangle\right] \tag{B1}
$$

where non-dimensional parameters m and n are a function shape parameters α and β indicating the shape of traction-separation. Parameters ϕ, and Γ are fracture energy and energy constant and Δ, and δ represents displacements and critical displacement for normal and shear separation.

The critical or final normal and shear opening width are

$$
\begin{aligned}
\delta_n &= \frac{\phi_n}{\sigma_n} \alpha\lambda_n(1 - \lambda_n)^{\alpha-1}\left(\frac{\alpha}{m} + 1\right)\left(\frac{\alpha}{m}\lambda_n + 1\right)^{m-1} \\
\delta_t &= \frac{\phi_t}{\sigma_t} \beta\lambda_t(1 - \lambda_t)^{\beta-1}\left(\frac{\beta}{n} + 1\right)\left(\frac{\beta}{n}\lambda_t + 1\right)^{n-1}
\end{aligned} \tag{B2}
$$

where λ_n and λ_t are initial slope indicator.

For equal normal and tangential fracture energies ($\phi_n = \phi_t$), energy constants are

$$
\Gamma_n = -\phi_n\left(\frac{\alpha}{m}\right)^m, \Gamma_t = \left(\frac{\beta}{n}\right)^n \tag{B3}
$$

Non-dimensional parameters m and n are

$$
m = \frac{\alpha(\alpha - 1)\lambda_n^2}{(1 - \alpha\lambda_n^2)}, n = \frac{\beta(\beta - 1)\lambda_t^2}{(1 - \beta\lambda_t^2)} \tag{B4}
$$

It is noted that the shape parameters control the softening region of traction-separation curve. If they are equal to 2, the shape of traction separation yields to linear triangular shape. The poten-
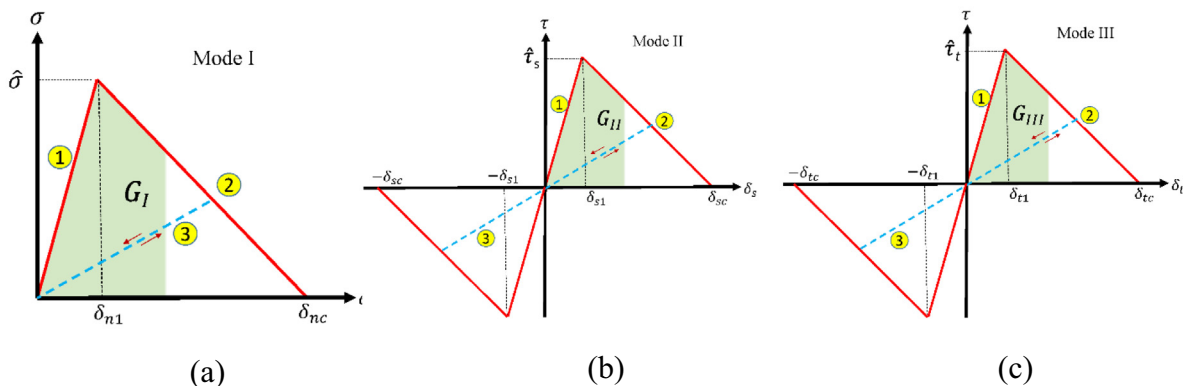

Fig. A1. The mode I (a), mode II (b), and mode III (c) traction-separation laws of the mixed-mode CZM used in this study.

tial based cohesive model implemented in UEL (user element) of ABAQUS by Ref. [61] is linked to 3D AFEM written in user element as well.

References

[1] Strouboulis T, Copps K, Babuska I. The generalized finite element method. Comput Methods Appl Mech Eng 2001;190(32–33):4081–193.
[2] Wells GN, Sluys LJ. A new method for modeling cohesive cracks using finite elements. Int J Numer Meth Eng 2001;50:2667–82.
[3] Moës N, Belytschko T. Extended finite element method for cohesive crack growth. Eng Fract Mech 2002;69:813–33.
[4] Moës N, Dolbow J, Belytschko T. A finite element method for crack growth without remeshing. Int J Numer Meth Eng 1999;46:131–50.
[5] Daux C, Moës N, Dolbow J, Sukumar N, Belytschko T. Arbitrary branched and intersecting cracks with the extended finite element method. Int J Numer Meth Eng 2000;48:1741–60.
[6] Huynh DBP, Belytschko T. The extended finite element method for fracture in composite materials. Int J Numer Meth Eng 2009;77:214–39.
[7] Areias PMA, Belytschko T. Analysis of the 3D crack initiation and propagation using the extended finite element method. Int J Numer Meth Eng 2005;63:760–88.
[8] Belytschko T, Gracia R, Ventura G. A review of extended/generalized finite element methods for material modeling. Int J Numer Meth Eng 2009;86:637–66.
[9] Song JH, Areias PMA, Belytschko T. A method for dynamic crack and shear band propagation with phantom nodes. Int J Numer Meth Eng 2006;67:868–93.
[10] Van de Meer FP, Sluys LJ. A phantom node formulation with mixed mode cohesive law for splitting in laminates. Int J Fract 2009;158:107–24.
[11] Remmers JJC, de Borst R, Needleman A. A cohesive segments method for the simulation of crack growth. Comput Mech 2003;31:69–77.
[12] Jager P, Steinmann P, Kuhl E. On local tracking algorithms for the simulation of three-dimensional discontinuities. Comput Mech 2008;42:395–406.
[13] Jager P, Steinmann P, Kuhl E. Modeling three-dimensional crack propagation — a comparison of crack path tracking strategies. Numer Meth Eng 2008:1328–52.
[14] Chen BY et al. A floating node method for the modelling of discontinuities in composites. Eng Fract Mech 2014:104–34.
[15] Ling DS, Yang QD, Cox BN. An augmented finite element method for modeling arbitrary discontinuities in composite materials. Int J Fract 2009;156:53–73.
[16] Liu W, Yang QD, Mohammadizadeh S, Su XY, Ling DS. An accurate and efficient augmented finite element method for arbitrary crack interactions. ASME J Appl Mech 2013;80(4):041033.
[17] Liu W, Yang QD, Mohammadizadeh S, Su X. Y. An efficient augmented finite element method (a-fem) for arbitrary cracking and crack interaction in solids. Int J Numer Methods Eng 2014;99(6):438–68.
[18] Naderi M, Jung J, Yang QD. A three dimensional augmented finite element for modeling arbitrary cracking in solids. Int J Frac 2016;197(147):168.
[19] Silling SA. Reformulation of elasticity theory for discontinuities and long-range forces. J Mech Phys Solids 2000;48:175–209.
[20] Rabczuk T, Bordas S, Zi G. A three-dimensional meshfree method for continuous multiple-crack initiation, propagation and junction in statics and dynamics. Comput Mech 2007;40:473–95.
[21] Bordas S, Rabczuk T, Zi G. Three-dimensional crack initiainitiation, propagation, branching and junction in non-linear materials by an extended meshfree method without asymptotic enrichment. Eng Fract Mech 2008;75:943–60.
[22] Rabczuk T, Bordas S, Zi G. On three-dimensional modelling of crack growth using partition of unity methods. Comput Struct 2010;88:1391–411.
[23] Zhuang XY, Augarde C, Bordas S. Accurate fracture modelling using meshless methods, the visibility criterion and level sets: formulation and 2D modelling. Int J Numer Meth Eng 2011;86:249–68.
[24] Duflot M. A meshless method with enriched weight functions for three-dimensional crack propagation. Int J Numer Meth Eng 2006;65:1970–2006.
[25] Barbieri E, Meo M. A meshfree penalty-based approach to delamination in composites. Compos Sci Technol 2009;69:2169–77.
[26] Holl M, Loehnert S, Wriggers P. An adaptive multiscale method for crack propagation and crack coalescence. Int J Numer Meth Eng 2013;93:23–51.
[27] Loehnert S, Mueller-Hoeppe DS, Wriggers P. 3D corrected XFEM approach and extension to finite deformation theory. Int J Numer Meth Eng 2011;86:431–52.
[28] Miehe C, Hofacker M, Welschinger F. A phase field model for rate-independent crack propagation: robust algorithmic implementation based on operator splits. Comput Methods Appl Mech Eng 2010;199:2765–78.
[29] Bourdin B, Francfort GA, Marigo JJ. The variational approach to fracture. J Elast 2008;91:5–148.
[30] Borden MJ, Verhoosel CV, Scotta MA, Hughes TJR, Landis C. A phase-field description of dynamic brittle fracture. Comput Methods Appl Mech Eng 2012;217–220:77–95.
[31] Belytschko T, Fish J, Engelmann BE. A finite element with embedded localization zones. Comput Methods Appl Mech Eng 1988;70(1):59–89.
[32] Alfaiate J, Wells GN, Sluys LJ. On the use of embedded discontinuity elements with crack path continuity for mode-I and mixed-mode fracture. Eng Fract Mech 2002;69:661–86.
[33] Ibrahimbegovic A, Melnyk S. Embedded discontinuity finite element method for modeling of localized failure in heterogeneous materials with structured mesh: an alternative to extended finite element method. Comput Mech 2007;40(1):149–55.
[34] Sluys LJ, Berends AH. Discontinuous failure analysis for mode-I and mode-II localization problems. Int J Solids Struct 1998;35:4257–74.
[35] Linder C, Armero F. Finite elements with embedded branching. Finite Elem Anal Des 2009;45:280–93.
[36] Linder C, Armero F. Finite elements with embedded strong discontinuities for themodeling of failure in solids. Int J Numer Meth Eng 2007;72:1391–433.
[37] Iarve EV, Gurvich MR, Mollenhauer D, Rose CA, Davila CG. Mesh independent matrix cracking and delamination modelling in laminated composites. Int J Numer Meth Eng 2011;88:749–73.
[38] Prabhakar P, Waas A. A novel continuum-decohesive finite element for modeling in-plane fracture in fiber reinforced composites. Compos Sci Technol 2013;83:1–10.
[39] Simo JC, Oliver J, Armero F. An analysis of strong discontinuities induced by softening solutions in rate-independent solids. J Comput Mech 1993;12:277–96.
[40] Gasser TC, Holzapfel GA. Modeling 3D crack propagation in unreinforced concrete using PUFEM. Comput Methods Appl Mech Eng 2005;194:2859–96.
[41] Mergheim J, Steinmann P. A geometrically nonlinear FE approach for the simulation of strong and weak discontinuities. Commun Numer Methods Eng 2006;195:5037–52.
[42] Gasser TC, Holzapfel GA. 3D crack propagation in unreinforced concrete. A two-step algorithm for tracking 3D crack paths. Comput Methods Appl Mech Eng 2006;195:5198–219.
[43] Krysl P, Belytschko T. Element free Galerkin method for dynamic propagation of arbitrary 3-D cracks. Int J Numer Meth Eng 1999;44(6):767–800.
[44] Rabczuk T, Belytschko T. Adaptivity for structured meshfree particle methods in 2D and 3D. Int J Numer Meth Eng 2005;63:1559–82.
[45] Feist C, Hofstetter G. Three-dimensional fracture simulations based on the SDA. Int J Numer Anal Meth Geomech 2007;31:189–212.
[46] Gasser TC. Validation of 3D crack propagation in plain concrete. Part II: Computational modeling and predictions of the PCT3D test. Comput Concr 2007;4:67–82.
[47] Oliver J, Huespe AE. On strategies for tracking strong discontinuities in computational failure mechanics. In: Proceedings of the Fifth World Congress on Computational Mechanics; 2002.
[48] Oliver J. Continuum approach to the numerical simulation of material failure in concrete. Int J Numer Meth Eng 2004;28:609–32.
[49] Duflot M. A study of the representation of cracks with level set. Int J Numer Meth Eng 2007;70:1261–302.
[50] Zhuang X, Augarde C, Mathisen KM. Fracture modeling using meshless methods and level sets in 3d: framework and modeling. Int J Numer Meth Eng 2012;92:969–98.
[51] Ventura G, Xu JX, Belytschko T. A vector level set method and new discontinuit approximations for crack growth by EFG. Int J Numer Meth Eng 2002;54:923–44.
[52] Chopp DL, Sukumar N. Fatigue crack propagation of multiple coplanar cracks with the coupled extended finite element/fast marching method. Int J Eng Sci 2003;41(8):845–69.
[53] Ferte G, Massin P, Moes N. 3D crack propagation with cohesive elements in the extended finite element method. Comput Method Appl Mech Eng 2016;300:347–74.
[54] Jager P, Steinmann P, Kuhl E. Modeling three-dimensional crack propagation— a comparison of crack path tracking strategies. Int J Numer Meth Eng 2008;76:1328–52.
[55] Felippa CA. Consistent node forces for the hpshel3 triangular shell element. Colorado: University of Colorado; 2000.
[56] Gálvez JC, Elices M, Guinea GV, Planas J. Mixed mode fracture of concrete under proportional and nonproportional loading. Int J Fract 1998;94:267–84.
[57] Galvez JC, Cend Gon D, Planas J, Guinea GV, Elices M. Fracture of concrete under mixed loading. Experimental results and numerical prediction. In: Fracture mechanics of concrete structures, proceedings FRAMCOS-3. Freiburg, Germany: AEDIFICATIO Publishers; 1998.
[58] Bocca P, Carpinteri A, Valente S. Size effects in the mixedmode crack propagation: softening and snap-back analysis. Eng Fract Mech 1990;35:159–70.
[59] Park K, Paulino GH. Cohesive zone models: a critical review of traction-separation relationships across fracture surfaces. Appl Mech Rev 2011;64:060802.
[60] Spring DW, Paulino GH. A growing library of three-dimensional cohesive elements for use in ABAQUS. Eng Fract Mech 2014;126:190–216.
[61] Park K, Paulino GH. Computational implementation of the PPR potential-based cohesive model in ABAQUS: educational perspective. Eng Fract Mech 2012;93:239–62.
[62] O'Higgins R, McCarthy MA, McCarthy CT. Comparison of open holetension characteristics of high strength glass and carbon fibre-reinforced composite materials. Compos Sci Technol 2008;68:2770–8.
[63] Zhou Y, YazdaniNezhad H, Hou C, Wan X, McCarthy MA, McCarthy CT. A three dimensional implicit finite element damage model and its application to single-lap multi-bolt composite joints with variable clearance. Compos Struct 2015;131:1060–72.

[64] Harper PW, Hallett SR. A fatigue degradation law for cohesive interface elements-development and application to composite materials. Int J Fatigue 2010;32(32):1774–87.

[65] Turon A, Dávila CG, Camanho PP, Costa J. An engineering solution for mesh size effects in the simulation of delamination using cohesive zone models. Eng Fract Mech 2007;74(10):1665–82.

[66] Harper PW, Hallett SR. Cohesive zone length in numerical simulations of composite delamination. Eng Fract Mech 2008;75(16):4774–92.

[67] Fang XJ, Zhou ZQ, Cox BN, Yang QD. High-fidelity simulations of multiple fracture processes in a laminated composites in tension. J Mech Phys Solids 2011;59:1355–73.